Flexible Asymmetric Supercapacitors Based upon Co_9S_8 Nanorod//Co_3O_4@RuO_2 Nanosheet Arrays on Carbon Cloth

Jing Xu,[†] Qiufan Wang,[†] Xiaowei Wang,[†] Qingyi Xiang,[†] Bo Liang,[†] Di Chen,[†,*] and Guozhen Shen[†,‡,*]

[†]Wuhan National Laboratory for Optoelectronics (WNLO) and School of Optical and Electronic Information, Huazhong University of Science and Technology (HUST), Wuhan 430074, China, and [‡]State Key Laboratory of Superlattices and Microstructures, Institute of Semiconductors, Chinese Academy of Sciences, Beijing 100083, China

ABSTRACT We have successfully fabricated flexible asymmetric supercapacitors (ASCs) based on acicular Co_9S_8 nanorod arrays as positive materials and Co_3O_4@RuO_2 nanosheet arrays as negative materials on woven carbon fabrics. Co_9S_8 nanorod arrays were synthesized by a hydrothermal sulfuration treatment of acicular Co_3O_4 nanorod arrays, while the RuO_2 was directly deposited on the Co_3O_4 nanorod arrays. Carbon cloth was selected as both the substrate and the current collector for its good conductivity, high flexibility, good physical strength, and lightweight architecture. Both aqueous KOH solutions and polyvinyl alcohol (PVA)/KOH were employed as electrolyte for electrochemical measurements. The as-fabricated ASCs can be cycled reversibly in the range of 0−1.6 V and exhibit superior electrochemical performance with an energy density of 1.21 mWh/cm^3 at a power density of 13.29 W/cm^3 in aqueous electrolyte and an energy density of 1.44 mWh/cm^3 at the power density of 0.89 W/cm^3 in solid-state electrolyte, which are almost 10-fold higher than those reported in early ASC work. Moreover, they present excellent cycling performance at multirate currents and large currents after thousands of cycles. The high-performance nanostructured ASCs have significant potential applications in portable electronics and electrical vehicles.

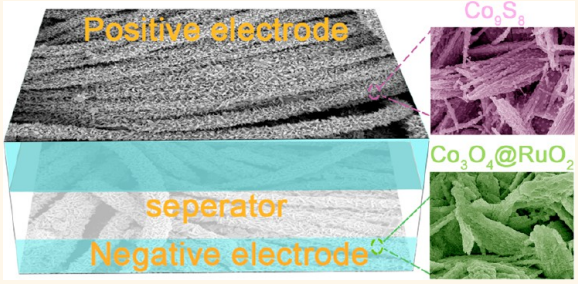

KEYWORDS: acicular nanorod · asymmetric supercapacitor · cobalt sulfide · flexible · RuO_2

Developing high-performance electrochemical energy storage devices has been one of the important issues in the strategic project proposed by the governments around the world.[1,2] Electrochemical capacitors (supercapacitors), with irreplaceable properties of high power density, fast charge−discharge rate (in seconds), and stable cycling performance, have become promising candidates in the energy storage areas, such as portable electronics and electrical vehicles. Although electric double-layer capacitors based on high surface area carbonaceous materials are widely used as commercial supercapacitors (SCs), faradaic pseudocapacitors with much higher specific capacitance are competitive for high-energy SC devices, such as transition-metal oxides, metal hydroxides, conductive polymers, metal sulfides, and their compounds.[3−14]

To meet the demands of high-performance energy storage, the energy density and output voltage of SCs should be improved without sacrificing the power density and cycle life.[15,16] According to the equation of energy density ($E = 0.5CV^2$), the specific energy of SCs can be improved by increasing the output voltage (V) and/or the specific capacitance (C).[17] To improve the voltage window of SCs, organic and ionic liquid electrolytes ($V \approx 3$ V) are usually employed, which suffer from the poor ionic conductivity, short cycle life, and toxicity. Another effectively alternative approach is to develop asymmetric supercapacitors (ASCs) based on the environmentally friendly aqueous electrolyte. For ASCs, by combining two electrodes with different voltage windows of charge storage *versus* the reference electrode, the sum output voltage up to 2 V can be supplied.[15−19] Intensive efforts have

* Address correspondence to gzshen@semi.ac.cn, dichen@mail.hust.edu.cn.

Received for review March 24, 2013 and accepted May 6, 2013.

Published online May 06, 2013
10.1021/nn401450s

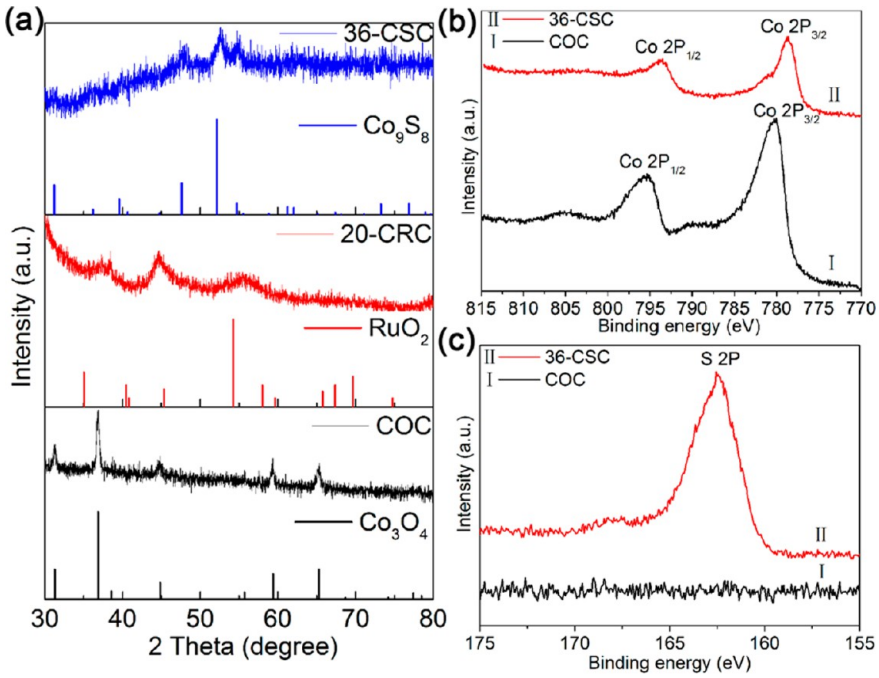

Figure 1. (a) XRD patterns of the as-synthesized COC, 20-CRC, and 36-CSC and the corresponding standard XRD patterns for Co_3O_4, RuO_2, and Co_9S_8. XPS patterns of (b) Co 2p and (c) S 2p of COC and 36-CSC.

been devoted to the ASCs with higher energy and power density by exploring various materials, such as $Ni(OH)_2$/graphene//graphene, MnO_2/graphene//carbon nanofibers, MnO_2//FeOOH, and so on.[15,18,19]

For weight, practicability, and portability reasons, SCs made of binder-free electrode materials grown on flexible conductive substrates, acting as new types of SCs, are more desirable for future electronics. For instance, Lu and co-workers fabricated a solid-state ASC based on H-TiO_2@MnO_2 (positive electrode) and H-TiO_2@C (negative electrode) grown on carbon cloth.[16] Chen *et al.* reported a transparent and flexible ASC by coating active materials on ITO-PET.[17] However, ASCs built on cobalt sulfides, a promising, environmentally friendly, and low-cost candidate, grown on a flexible conductive substrate have not been studied yet.[10,20] As one-dimensional (1D) Co_3O_4 nanostructures can be synthesized through a facile hydrothermal method, it may be a favorable precursor for synthesizing cobalt sulfides by S^{2-} ion exchange.[21] Such a process also overcomes the difficulty of growing cobalt sulfides in the 1D direction.[20,22] Meanwhile, Co_3O_4 nanorods with high specific area could also be used as scaffolds to support the negative electrode materials, such as carbon materials, FeOOH, RuO_2, and so on.[1,5,19]

On the basis of the above ideas and the structure engineering of electrodes, we report in this work the fabrication of an interesting asymmetric supercapacitor with cobalt sulfides grown on woven carbon cloth as positive electrode and Co_3O_4 nanowires arrays/RuO_2 nanosheet-based composition as negative electrode. Acicular Co_3O_4 nanorod arrays grown on woven carbon cloth (denoted as COC) by facile hydrothermal reactions were used as both the precursor for Co_9S_8 nanorod arrays (*t*-CSC, *t* represents the sulfuration time, in hours) and the scaffolds for RuO_2 nanosheets (*t*-CRC, *t* represents the compositing time, in hours). Our optimized ASCs showed a volumetric capacitance as high as 3.42 F/cm^3 in aqueous electrolyte and 4.28 F/cm^3 in PVA/KOH electrolyte, both delivering an output voltage of 1.6 V. Expectably, excellent performances with an energy density of 1.21 mWh/cm^3 at the power density of 13.29 W/cm^3 for liquid-state ASC and an energy density of 1.44 mWh/cm^3 at the power density of 0.89 W/cm^3 for solid-state ASC were achieved, respectively, which are around 10-fold larger than some reported ASCs.[16,23−25]

RESULTS AND DISCUSSION

Figure 1a shows the X-ray diffraction (XRD) patterns of the as-prepared samples under different conditions. All peaks of the COC sample excluding the one coming from the carbon cloth can be indexed to a cubic spinel phase of Co_3O_4 (JCPDS Card No. 42-1467). In the XRD pattern of the 36-CSC (acicular Co_9S_8 nanorod arrays obtained after 36 h of sulfuration in Na_2S solution), only the peaks of Co_9S_8 can be observed, according to JCPDS Card No. 86-2273. The broad reflection peaks and the noise may be aroused by the poor crystallinity of the 36-CSC. The diffraction pattern of 20-CRC (Co_3O_4@RuO_2) is also shown. Only three broad peaks can be observed excluding the typical peak of carbon cloth at 25°, which could be indexed to the standard XRD pattern of Co_3O_4 at 36.8° and RuO_2 with JCPDS Card No. 18-1139. The broadened peaks indicate the small size of the deposited RuO_2 nanocrystals. X-ray

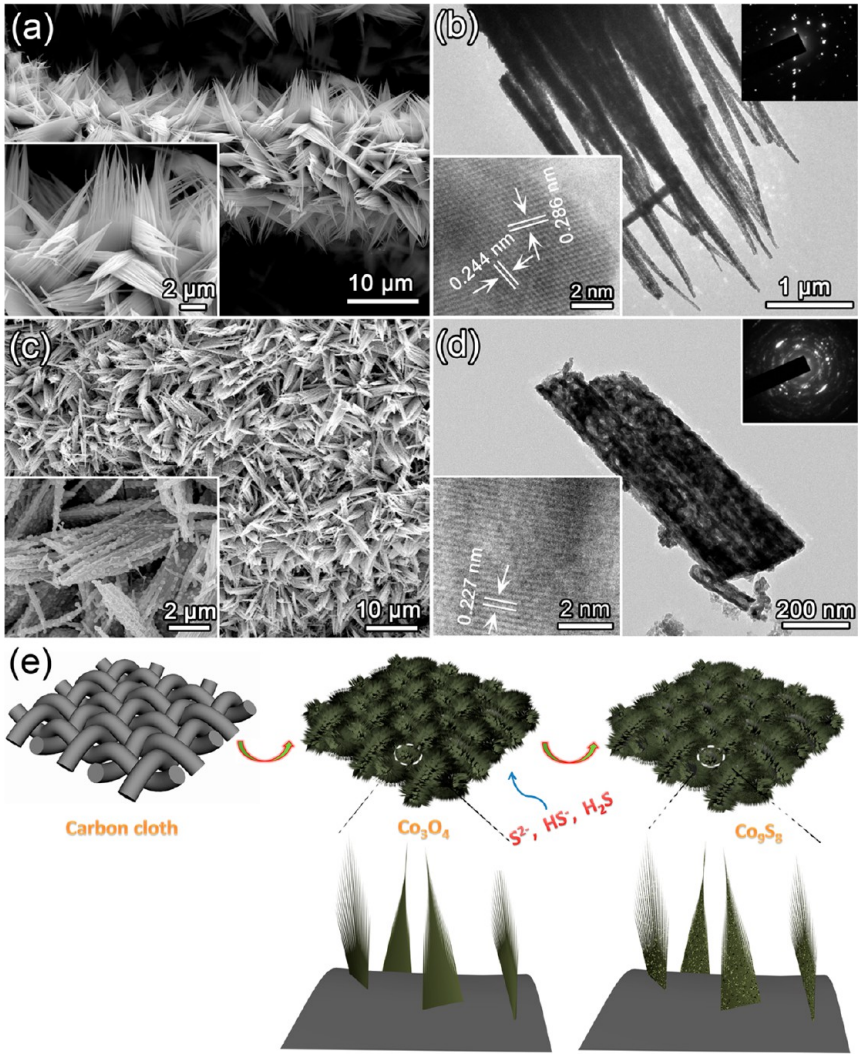

Figure 2. (a) SEM images and (b) TEM images of COC with a SAED pattern of the COC sample. (c) SEM images and (d) TEM images of the 36-CSC sample with a SAED pattern. (e) Mechanism of the conversion process from COC to CSC.

photoelectron spectroscopy (XPS) analysis was applied to further verify the surface compositions of the COC and the 36-CSC samples. High-resolution spectra of Co 2p and S 2p are exhibited in Figure 1b,c. The XPS spectrum of COC for Co 2p in Figure 1b presents two major peaks with binding energies of 780.2 and 795.2 eV with a spin energy of 15 eV, corresponding to the Co $2p_{3/2}$ and Co $2p_{1/2}$ of Co_3O_4 phase, respectively.[21] In the case of 36-CSC, the peaks of Co $2p_{3/2}$ and Co $2p_{1/2}$ are located at 778.4 and 793.5 eV, which agrees with the reports very well.[20,26] In Figure 1c, no S 2p peak was found in the spectrum of COC, indicating nonexistance of sulfide in COC. Meanwhile, the strong peak of S 2p at 162.6 eV in the pattern of 36-CSC manifests the formation of Co_9S_8 further.[20,27]

Scanning electron microscopy (SEM) and transmission electron microscopy (TEM) are employed to investigate the morphologies and microstructures of the COC and 36-CSC samples, as shown in Figure 2. It can be seen that the COC sample composed of 1D acicular nanorods with a smooth surface aligned together to form a leaf, arranging randomly on the carbon fibers (Figure 2a). TEM image in Figure 2b exhibits that the Co_3O_4 nanorods possess porous structure with good crystallinity, as revealed by the SAED pattern. A high-resolution TEM (HRTEM) image at the bottom left of the figure reveals the lattice fringe spacings of 0.286 and 0.244 nm, corresponding well to the (220) and (311) crystal planes of the cubic spinel Co_3O_4 phase, respectively. After being treated with Na_2S for 12 h (12-CSC), the surface of the Co_3O_4 nanorods becomes a little bit rough, as shown in Supporting Information Figure S1a,b. Figure S1c,d shows the surface morphology of the 24-CSC sample, where many nanoparticles are formed on the surface of the nanorods and make them much rougher than the 12-CSC sample. By extending the sulfuration time to 36 h (36-CSC), more nanoparticles are coated on the surface while the 1D acicular rods and 3D leaf morphologies still remain, as shown in Figure 2c. Figure 2d presents the TEM images of the 36-CSC sample, from which the porous structure can be observed clearly. The lattice fringe spacing of 0.227 nm

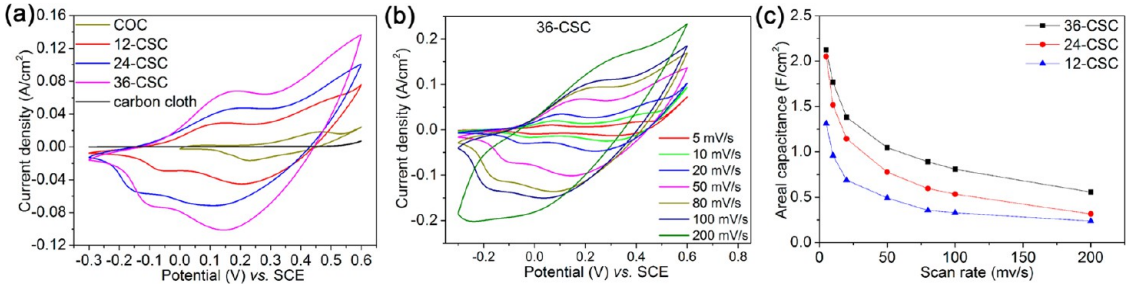

Figure 3. (a) CV curves of COC, 12-CSC, 24-CSC, 36-CSC, and the pure carbon cloth electrodes at the scan rate of 50 mV/s. (b) CV curves of 36-CSC at different scan rates. (c) Specific areal capacitance of 12-CSC, 24-CSC, and 36-CSC electrodes calculated from the CV curves as a function of scan rates.

can be indexed as the (331) lattice plane of Co_9S_8. SAED pattern at the top right corner indicates the polycrystalline structure of the sample. In Figure S1e, the energy-dispersive spectrometer (EDS) microanalysis of 36-CSC sample reveals that Co and S elements dominate in the compound with the ratio approaching 1:1, further verifying the formation of Co_9S_8. According to the results above, a possible mechanism is exhibited in Figure 2e. When acicular Co_3O_4 nanorod arrays are grown on flexible carbon cloth successfully, S^{2-}, HS^-, and H_2S in Na_2S solution react with Co_3O_4 by permeating into the nanorods through nanopores. The ion-exchange reaction occurs slowly to convert all of the Co_3O_4 to Co_9S_8 homogeneously and keep the morphology. As the concentration of sulfide ions on the surface of nanorods is higher than that inside, cobalt ions on the surface react with sulfide ions *in situ* violently, leading to the formation of some nanoparticles on the surface.

The electrochemical studies for the COC and CSC samples were conducted in a three-electrode cell in 3 M KOH aqueous electrolyte, with a Pt counter electrode and a SCE reference electrode. Figure 3a shows the cyclic voltammogram (CV) curves of the COC, 12-CSC, 24-CSC, 36-CSC, and the pure carbon cloth electrodes at the scan rate of 50 mV/s. As expected, the pure carbon electrode contributes little to the capacitance of the electrodes, and the CSC electrodes exhibit much higher current densities and larger voltage range than those of the COC electrode, indicating substantial improvement of electrochemical capacitance by sulfuration. Moreover, the CSC electrodes show a linear increased performance dependent on the sulfuration time. In Figure 3b, a series CV curves of the 36-CSC sample with stable potential window of −0.3−0.6 V at different scan rates were collected, illustrating the typical pseudocapacitive mechanism according to the redox peaks. Two possible reactions are proposed for the electrochemical reactions:[10,28,29]

$$Co_9S_8 + OH^- \leftrightarrow Co_9S_8OH + H_2O + e^- \quad (1)$$

$$Co_9S_8OH + OH^- \leftrightarrow Co_9S_8O + H_2O + e^- \quad (2)$$

The areal capacitances of the 12-CSC, 24-CSC, and 36-CSC samples were calculated at scan rates of 5 to 200 mV/s with a decreased trend dependent on the scan rates, owing to the limited rate of ion diffusion at high scan rates, as shown in Figure 3c. The highest capacitance value obtained from 36-CSC was 2.35 F/cm^2 (783.3 F/g for active materials and 113.5 F/g for the overall electrode) at 5 mV/s, which is much better than previously reported data about active materials grown on substrates and some cobalt sulfides.[20,29−31] Even at a high scan rate of 200 mV/s, the 36-CSC electrode still yielded a high capacitance of 0.56 F/cm^2. Additionally, galvanostatic measurements of 36-CSC are displayed in Figure S2a, again confirming the stable potential output and high areal capacitance of 0.86 and 0.84 F/cm^2 at large current densities of 10 and 50 mA/cm^2, respectively. Furthermore, the 36-CSC sample presented excellent capacitance stability (92.0% retention) after being charge−discharged at the current density of 10 mA/cm^2 (Figure S2b). The SEM images of the 36-CSC electrode after the cycling test are shown in Figure S2c,d. It is seen that the sample remained as an acicular rod-leaf structure, while some nanosheets were formed on the surface of the nanorod, which may be ascribed for the two-dimensional growth trend of the intermediate product (Co_9S_8OH) formed during the pseudocapacitive reaction.[22] This modified structure may be benificial to enhance the specific area while cause some interface resistance. Thus, these results convincingly demonstrate that the 36-CSC sample is a promising electrode for electrochemical energy storage.

RuO_2 has emerged as a promising material for application in electrochemical supercapacitors. Here we developed a Co_3O_4@RuO_2 hybrid structure on carbon cloth as negative electrode to couple with the 36-CSC electrode. SEM images of the Co_3O_4@RuO_2 reacted for 20 h (20-CRC) are displayed in Figure 4a. Dense RuO_2 nanoparticles were deposited on the surface of the Co_3O_4 nanorods and changed the rod-assembled leaves into porous sheets, which is beneficial for enlarging the specific area to store more charges. As shown in Figure 4b, RuO_2 nanoparticles with a diameter of around 30 nm formed a porous structure. The HRTEM image in the inset shows clearly resolved lattice fringe spacings of 0.274 and 0.244 nm, in line with the (111) and (200) crystal planes of RuO_2, respectively. The SAED pattern shown in the inset

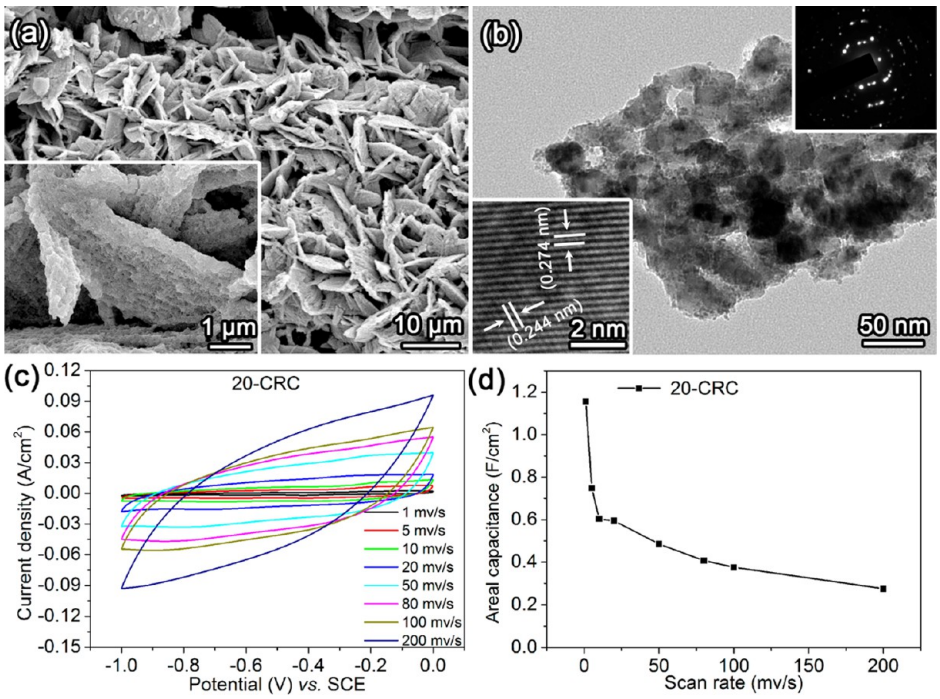

Figure 4. (a) SEM images and (b) TEM images of the 20-CRC sample with a SAED pattern. (c) CV curves at different scan rates. (d) Specific areal capacitance calculated from the CV curves as a function of scan rates.

confirms the well-crystallized structure of the RuO_2 nanoparticles. Energy-dispersive X-ray spectroscopy mapping shown in Figure S3a provides clearer information about the element distribution within the hybrid nanostructures, which further confirms the formation of the composited Co_3O_4@RuO_2 structures. The electrochemical performance of the CRC electrodes was evaluated in the three-electrode configuration in 3 M KOH. Figure S3b shows the CV curves of the 6-CRC, 12-CRC, 20-CRC, and 26-CRC samples at the scan rate of 50 mV/s in the voltage range of −1−0 V, indicating that the largest CV integrated area belongs to the composited Co_3O_4@RuO_2 reacted for 20 h (20-CRC). CV curves for the 20-CRC sample at different scan rates from 1 to 200 mV were recorded to calculate the electrochemical capacitance of the electrode (Figure 4c), which is plotted in Figure 4d. Capacitances of 1.18 F/cm^2 (590 F/g calculated by the total mass (2 mg/cm^2) of the Co_3O_4 and RuO_2 and 59.9 F/g based on the overall mass of the electrode) at 1 mV/s and 0.29 F/cm^2 at 200 mV/s can be achieved. Galvanostatic charge−discharge measurements of the 20-CRC electrode were also conducted, as shown in Figure S4a. The areal capacitances of 0.67 and 0.39 F/cm^2 were obtained at current densities of 10 and 50 mA/cm^2, respectively, which are comparable with those calculated by the CV curves. Moreover, the capacitance retention of 89.1% after being cycled for 2000 times at a current density of 10 mA/cm^2 (Figure S4b) proves the 20-CRC electrode to be good candidate for negative electrode in ASCs, as well. Figure S4c exhibits the SEM image of the 20-CRC electrode after being cycled, and some cracks were observed, which may cause some electrode disconnection of the material with conductive fibers. Significantly, these results are better than those of some other active materials used as negative electrodes.[16,32,33]

Given that the 36-CSC and 20-CRC electrodes possess stable voltage windows between −0.3 and 0.6 V and between −1 and 0 V, respectively, with regard to the SCE, it is expected that the operating ASC voltage could achieve 1.6 V in 3 M KOH by assembling the 36-CSC electrode with the 20-CRC electrode. Taking advantage of good flexibility and conductivity of carbon cloth, we fabricated an all solid-state ASC in PVA/KOH gel electrolyte. Figure 5a displays the schematic illustration of the assembled structure for such ASCs. The electrochemical performance of liquid-state and solid-state ASCs were both studied. Figure 5b shows the CV curves of the liquid-state ASC (denoted as LASC) at different voltage windows. As expected, the stable electrochemical windows of the LASC can be extended to 1.6 V. In Figure 5c, CV curves at different scan rates were collected from 10 mV/s, and the typical faradaic pseudocapacitive shape was robust enough even at the scan rate up to 1000 mV/s, indicating the stability of the LASC at fast charge−discharge rates. On the other hand, the voltage window of solid-state ASC (denoted as SASC) can also achieve 1.6 V and perform well even at the high scan rate of 1000 mV/s, as shown in Figure 5d,e. Due to the different ion diffusion rate in the liquid electrolyte and the solid electrolyte, the CV shape of the SASC differs with that of LASC. In order to evaluate the potential of the SASC for flexible energy storage under real conditions, the CV curves of the device at 100 mV/s were collected under normal, bent,

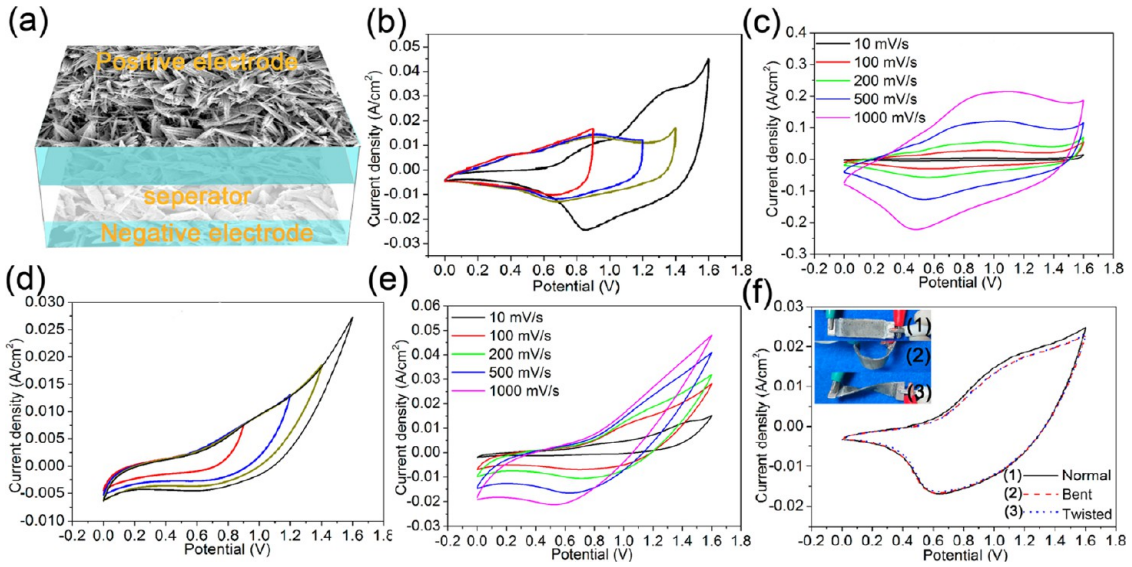

Figure 5. (a) Schematic illustration of the as-assembled ASC. (b,d) CV curves of the LASC and SASC devices collected in different scan voltage windows at the scan rate of 50 mV/s. (c,e) CV curves of the LASC and SASC devices collected at different scan rates. (f) CV curves collected at the scan rate of 100 mV/s for the solid-state ASC device under normal, bent, and twisted conditions. Insets are the device photographs under different test conditions.

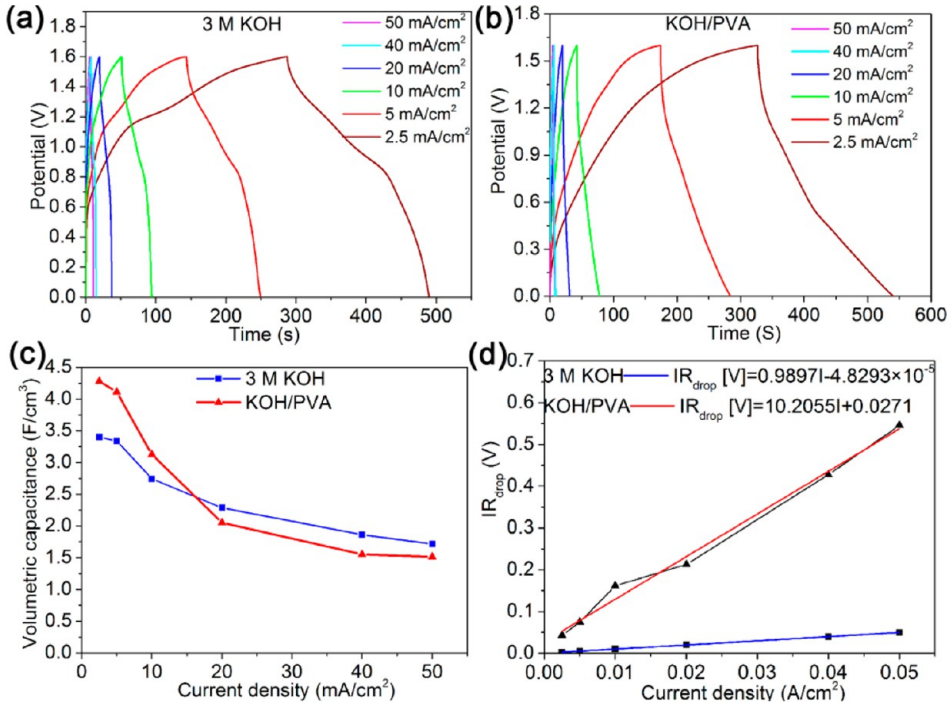

Figure 6. (a,b) Galvanostatic charge–discharge curves collected at different current density for LASC and SASC devices in the voltage window of 1.6 V. (b) Volumetric capacitance of LASC and SASC devices collected from galvanostatic charge–discharge curves as a function of current density. (c) Voltage drop associated with the cell internal resistance (IR loss) *vs* discharge current density and corresponding fitted functions.

and twisted conditions, revealing its excellent mechanical stability.

To further confirm the superior electrochemical performance of both kinds of ASCs, the galvanostatic charge–discharge measurements were conducted, as shown in Figure 6a,b. A set of current densities of 2.5, 5, 10, 20, 40, and 50 mA/cm^2 were operated. At each current density, both ASCs charge and discharge rapidly with good electrochemical reversibility with a stable potential window of 0–1.6 V. Figure 6c calculates the volumetric capacitances of the ASCs based on the charge–discharge curves. Significantly, the specific capacitance of SASC exhibits higher values at small current densities. While at larger current densities, the

LASC shows slower decay with increasing the current density than the SASC. The tiny difference between the LASC and SASC can be accounted for the following two reasons: (1) device volume of SASC is smaller than that of LASC because of the thinner thickness of KOH/PVA than that of glass fiber used as separator in LASC; (2) ion conductivity in polymer is poorer than that in aqua, which would limit the rate of charge collected at large current densities. By thinning both kinds of separators, better performance can be expected. In our work, the volumetric capacitance of the as-fabricated LASC device achieves 3.42 F/cm^3 at 2.5 mA/cm^2 and that of SASC is as high as 4.28 F/cm^3, which is more than 5 times greater than that of the latest reports about LASC and SASC, respectively.[16,23,24] The voltage drops of both ASCs *versus* current density are plotted in Figure 6d, and corresponding liner functions are fitted. Obviously, LASC shows much smaller internal resistance than SASC according to the gentle slope, which can be ascribed for the better conductivity of aqueous electrolyte than polymers.[2]

The electrochemical impedance spectroscopy (EIS) analysis has been recognized as one of the principal methods for examining the fundamental behavior of supercapacitors. For further comparison, EIS of both ASCs was measured in the frequency range of 100 kHz to 0.01 Hz with an ac perturbation of 5 mV (Figure S5). In Figure S5a, the intercepts of the Nyquist curves on the real axis are about 0.4 and 2.7 Ω for LASC and SASC, respectively, manifesting the good conductivity of the electrolyte and very low internal resistance of the electrode, on the same magnitude with the slope values fitted in Figure 6d. The approximate nonexistence of the semicircle in the high-frequency region of LASC illustrates good charge transfer conductivity of the device at the electrolyte−electrode interface. On the other hand, the charge transfer resistance of SASC is about 0.5 Ω according to the equivalent circuit shown in the inset of Figure S5a, which is even smaller than that of SCs with aqueous electrolytes reported.[34] In the Bode plots of the as-fabricated devices displayed in Figure S5b, the characteristic frequencies f_o for a phase angle of −45° are 2.49 Hz (LASC) and 0.18 Hz (SASC). This frequency marks the point at which the resistive and capacitive impedances are equal.[23] The corresponding time constants τ_o (=1/f_o) are calculated to be 0.40 and 5.55 s, showing rapid frequency response than some conventional active-carbon-based SCs (about 10 s).[23] The phase angle of LASC at 10 mHz is about −82°, which is better than that of some commercial activated carbon supercapacitors.[20] Generally, the excellent EIS performance of the ASCs can be accounted by the large and accessible surface area of materials and binder-free structures of the electrode.

The electrochemical stability of both devices was evaluated through a cyclic charge−discharge process. Figure 7a reveals the current density dependence of

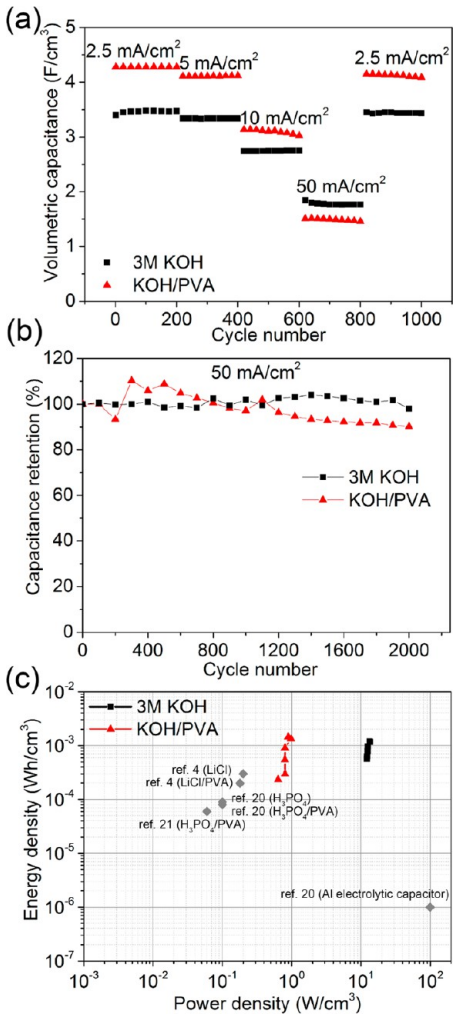

Figure 7. (a) Rate capability of LASC and SASC at different current densities. (b) Cycling performance of LASC and SASC devices at the current density of 50 mA/cm^2 for 2000 cycles. (c) Ragone plots of LASC and SASC devices. The values reported for other SC devices are added for comparison.

the cycling performance. During the process, five steps of charge−discharge rates were changed successively from 2.5 to 50 mA/cm^2. At the first 400 cycles with charge−discharge current densities of 2.5 and 5 mA/cm^2, both ASCs show steady volumetric capacitances. In the following 400 cycles at large current densities, the LASC demonstrates a stable performance at each situation while the SASC shows a little decay. When the current turns back to 2.5 mA/cm^2, a fully recovered LASC is observed in the following 200 cycles while the retention capacitance of SASC is calculated to be 95.6%. The long-term cycling performance of the ASC devices at a large charge−discharge rate (50 mA/cm^2, namely, 10 A/g based on the total mass of Co_9S_8, Co_3O_4, and RuO_2) was also conducted for 2000 cycles. The LASC exhibits excellent stability with even 99.0% retention of the initial capacitance and the SASC remains at 90.2%. These retention rates at such a high charge−discharge rate are comparable and even better than those reported for

other aqueous and solid-state SCs, such as MnO_2/CNT// MnO_2/CNT (aqueous, 65% after 2000 retention),[35] H-TiO_2@MnO_2//H-TiO_2@C (aqueous, 89% after 2000 cycles; $LiCi_4$/PVA, 96% after 2000 cycles at around 5 mA/cm^2),[16] $Ni(OH)_2$/CNT//active carbon (aqueous, 88% after 2000 cycles at 50 mA/cm^2),[33] PPy/nanoporous gold//PPy/nanoporous gold ($HClO_4$/PVA, 78% after 1000 cycles at 0.05 mA/cm^2),[36] RuO_2/graphene//graphene (H_2SO_4/PVA, 95% after 2000 cycles at 1A/g).[37]

The power density (*P*) and energy density (*E*) are generally used as important parameters to characterize the performance of electrochemical cells. Although it is a challenge to compare the performance of all types of supercapacitors due to a lot of variables such as structures of electrodes, material mass loadings, charge–discharge rates, and test configurations, a rough comparison can still be made through the Ragone plot, as shown in Figure 7c. The maximum energy density of 1.21 mWh/cm^3 was obtained at the power density of 13.29 W/cm^3 for LASC, which is more than 10-fold higher than those in some latest papers that employed an aqueous electrolyte, such as H-TiO_2@MnO_2//H-TiO_2@-C-based ASCs (0.3 mWh/cm^3 at 0.2 W/cm^3, 5 M LiCl)[16] and graphene-based SCs (0.09 mWh/cm^3 at 0.1 W/cm^3, 1 M H_3PO_4).[23] Moreover, although the calculated volumetric energy and power of SASC (1.44 mWh/cm^3 at the power density of 0.89 W/cm^3) are lower than the LASC, which are still about 5 times higher than the reported values of some SASC, including the solid-state H-TiO_2@MnO_2// H-TiO_2@C SCs with 0.2 mWh/cm^3 at 0.18 W/cm^3 (PVA/LiCl), graphene-based SCs with 0.08 mWh/cm^3 at 0.1 W/cm^3 (PVA/H_3PO_4), MnO_2/carbon nanoparticle-based SCs with 0.06 mWh/cm^3 at 0.06 W/cm^3 (PVA/H_3PO_4), and CNT-based supercapacitors with 0.13 mWh/cm^3 at 0.73 W/cm^3 (ionic-liquid-based gel electrolytes).[24,25] The excellent performance of the as-fabricated ASCs can be attributed to the following reasons: (1) woven and porous structure of carbon cloth is beneficial for the growth of active materials on a large scale and the diffusion of electrolyte ions; (2) hybrid structure of 36-CSC and 20-CRC electrodes provides large accessible area for pseudocapacitive reaction and double-layer charge storage; (3) the binder-free electrodes enables a low internal resistance and fast electrode–electrolyte charge transfer.

CONCLUSION

High-performance asymmetric supercapacitors were demonstrated with acicular Co_9S_8 arrays as positive electrode and Co_3O_4@RuO_2 nanosheet arrays as anode materials on woven carbon fabrics. Both liquid-state and solid-state ASCs show stable output voltage of 1.6 V and provide high volumetric capacitance of 3.42 and 4.28 F/cm^3, excellent electrochemical performance of 1.21 mWh/cm^3 at 13.29 W/cm^3 with aqueous electrolyte and 1.44 mWh/cm^3 at 0.89 W/cm^3 with solid-state electrolyte. Moreover, stable rate capability and cycle capability were also achieved. These encouraging findings can open up the possibility of sulfide composites for applications in asymmetric supercapacitors with high voltage, high energy, and high power densities to meet the diverse demands in industry development.

METHODS

Synthesis of COC. All chemicals were used without any purification. Prior to the synthesis, a piece of carbon cloth (2 cm × 8 cm) was cleaned by acetone, ethanol, and distilled water in sequence. In a typical synthesis, 2 mmol of $CoCl_2 \cdot 6H_2O$, 4 mmol of $CO(NH_2)_2$ and 10 mmol of NH_4F were dissolved in 30 mL of DI water under stirring at room temperature. After stirring for 30 min, the homogeneous solution was transferred into a 50 mL autoclave and the cleaned carbon cloth was immersed into the solution around the autoclave wall. The autoclave was sealed and heated at 120 °C for 10 h in an electric oven. When the autoclave was cooled to room temperature, the carbon cloth coated with purple precursor was picked out and washed with DI water. Finally, the precursor on the carbon cloth was annealed at 400 °C for 1 h, and black Co_3O_4 on the carbon cloth was obtained.

Synthesis of CSC. A piece of COC (1 cm × 8 cm) was soaked in a 25 mL solution containing 1 g of Na_2S in a 50 mL autoclave. After being sealed, the autoclave was heated at 120 °C for various hours (*i.e.*, 12, 24, and 36 h). Then, the converted sample was washed with distilled water and dried at 50 °C under vacuum.

Synthesis of CRC. CRC was obtained by immersing a piece of COC (1 cm × 8 cm) in a 12 mL solution containing 0.06 g of $RuCl_3 \cdot H_2O$ in a 50 mL autoclave. After being heated at 180 °C for various hours (*i.e.*, 6, 12, 20, and 26 h), the as-prepared sample was washed with distilled water and then annealed at 150 °C for 2 h.

Fabrication of Liquid-State ASCs (LASC). Aqueous ASCs were assembled by a piece of 36-CSC (1 × 1 cm^2) and a piece of 20-CRC (1 × 1 cm^2) with a glass fiber separator in two-electrode simulation cells. A KOH solution (3 M) was employed as the electrolyte. The thickness of the device was measured to be 1 mm, including the electrodes and the separator.

Fabrication of Solid-State ASCs (SASC). Solid-state ASCs were assembled by separating the 36-CSC and the 20-CRC with solid-state PVA/KOH electrolyte. The PVA/KOH gel electrolyte was prepared by dissolving 6 g of PVA and 4.5 g of KOH in 60 mL of water at 90 °C under vigorous stirring for 1 h. Before assembling, each electrode was coated with PVA/KOH gel and then allowed to solidify at room temperature for 1 h. Finally, the electrodes were sandwiched together by PVA/KOH gel and left overnight until the electrolyte solidified. In the SASC, the polymer electrolyte acts as both the electrolyte and the ion-porous separator. The thickness of the solid-state ASC was measured to be 0.8 mm.

Materials Characterizations and Electrochemical Measurements. The chemical composition, morphology, and the microstructure of the samples were characterized by X-ray diffraction patterns (XRD, X'Pert PRO, PANalytical B.V., The Netherlands) with radiation from a Cu target (Kα, λ = 0.15406 nm), field emission scanning electron microscopy (FESEM; JEOL JSM-6700F, 5 kV), transmission electron microscopy (HRTEM; JEOL, JEM-2010 HT), and XPS (VG Multilab 2000 system with a monochromatic Al Kα X-ray source). CV, galvanostatic charge–discharge measurements, electrochemical impedance spectroscopy (EIS, 100 kHz–0.01 Hz, 5 mV amplitude), and cycling performance measurements were conducted using an electrochemical workstation (CHI 760D). The electrochemical studies of the individual electrode were performed in a three-electrode cell, with a Pt counter electrode and a SCE reference electrode. The measurements of aqueous ACSs were conducted in two-electrode stainless steel simulation cells.

Calculations. The capacitance (C) and areal capacitance (C_A) of each electrode in the three-electrode configuration are calculated from the CV curves at different scan rates using the formula

$$C = (\int i\mathrm{d}V)/\nu(\Delta V) \quad (1)$$

$$C_A = C/A \quad (2)$$

where i (in amps, A) is the response current, ν is the potential scan rate (V/s), and ΔV is the applied potential region (in volts, V). Specific capacitances were calculated based on the area of the electrode, where A refers to the area (cm^2) of the electrode.

The capacitance (C) and volume capacitance (C_V) of each device in the two-electrode configuration are calculated from the galvanostatic charge−discharge curves using the formula

$$C = i/(-\mathrm{d}V/\mathrm{d}t) \quad (3)$$

$$C_V = C/V \quad (4)$$

where i (in amps, A) is the applied current, $\mathrm{d}V/\mathrm{d}t$ is the slope of the discharge curve (in volts per second, V/s), and V is the volume (cm^3) of the device.

The areal energy density (E) in Wh/cm^3 and power density (P) in W/cm^3 derived from galvanostatic charge−discharge curves are calculated from the following expressions:

$$E = C(\Delta E)^2/(2V \times 3600) \quad (5)$$

where ΔE is the operating voltage window (measured in volts and obtained from the discharge curve excluding the voltage drop)

$$P = \Delta E^2/(4RV) \quad (6)$$

where R ($=V_{drop}/2i$) is the internal resistance of the device that is estimated from the voltage drop (V_{drop}) at the beginning of the discharge curve.

Conflict of Interest: The authors declare no competing financial interest.

Acknowledgment. This work was supported by the National Natural Science Foundation (51002059, 21001046, 91123008), the 973 Program of China (2011CB933300), the Program for New Century Excellent Talents of the University in China (Grant No. NCET-11-0179), and the Natural Science Foundation of Hubei Province (2011CDB035). Special thanks to the Analytical and Testing Center of HUST and the Center of Micro-Fabrication and Characterization (CMFC) of WNLO for using their facilities.

Supporting Information Available: SEM images for 12-CSC and 24-CSC, EDS result for 36-CSC, galvanostatic charge−discharge curves, cycling performance and SEM images after being cycled of 36-CSC electrode, CV curves for different CRC electrodes, galvanostatic charge−discharge curves, cycling performance and SEM image after cycling test of 20-CRC electrode, electrochemical impedance measurements. This material is available free of charge *via* the Internet at http://pubs.acs.org.

REFERENCES AND NOTES

1. US Department of Energy, Basic Research Needs for Electrical Energy Storage 2007; www.sc.doe.gov/bes/reports/abstracts.html#EES (accessed February 2010).
2. Izadi-Najafabadi, A.; Yasuda, S.; Kobashi, K.; Yamada, T.; Futaba, D. N.; Hatori, H.; Yumura, M.; Iijima, S.; Hata, K. Extracting the Full Potential of Single-Walled Carbon Nanotubes as Durable Supercapacitor Electrodes Operable at 4 V with High Power and Energy Density. *Adv. Mater.* **2010**, *22*, E235–E241.
3. Liu, J.; Jiang, J.; Bosman, M.; Fan, H. J. Three-Dimensional Tubular Arrays of MnO_2-NiO Nanoflakes with High Areal Pseudocapacitance. *J. Mater. Chem.* **2012**, *22*, 2419–2426.
4. Wang, Q.; Liu, B.; Wang, X.; Ran, S.; Wang, L.; Chen, D.; Shen, G. Morphology Evolution of Urchin-like $NiCo_2O_4$ Nanostructures and Their Applications as Pseudocapacitors and Photoelectrochemical cells. *J. Mater. Chem.* **2012**, *22*, 21647–21653.
5. Wang, H.; Liang, Y.; Mirfakhrai, T.; Chen, Z.; Casalongue, H.; Dai, H. Advanced Asymmetrical Supercapacitors Based on Graphene Hybrid Materials. *Nano Res.* **2011**, *4*, 729–736.
6. Guan, C.; Liu, J.; Cheng, C.; Li, H.; Li, X.; Zhou, W.; Zhang, H.; Fan, H. J. Hybrid Structure of Cobalt Monoxide Nanowire@ Nickel Hydroxidenitrate Nanoflake Aligned on Nickel Foam for High-Rate Supercapacitor. *Energy Environ. Sci.* **2011**, *4*, 4496–4499.
7. Niu, Z. Q.; Luan, P. S.; Shao, Q.; Dong, H. B.; Li, J. Z.; Chen, J.; Zhao, D.; Cai, L.; Zhou, W. Y.; Chen, X. D.; *et al.* A "Skeleton/Skin" Strategy for Preparing Ultrathin Free-Standing Single-Walled Carbon Nanotube/Polyaniline Films for High Performance Supercapacitor Electrodes. *Energy Environ. Sci.* **2012**, *5*, 8726–8733.
8. Liu, H.; Su, D.; Zhou, R.; Sun, B.; Wang, G.; Qiao, S. Z. Highly Ordered Mesoporous MoS_2 with Expanded Spacing of the (002) Crystal Plane for Ultrafast Lithium Ion Storage. *Adv. Energy Mater.* **2012**, *2*, 970–975.
9. Shi, W.; Zhu, J.; Rui, X.; Cao, X.; Chen, C.; Zhang, H.; Hng, H. H.; Yan, Q. Controlled Synthesis of Carbon-Coated Cobalt Sulfide Nanostructures in Oil Phase with Enhanced Li Storage Performances. *ACS Appl. Mater. Interfaces* **2012**, *4*, 2999–3006.
10. Chen, C.-Y.; Shih, Z.-Y.; Yang, Z.; Chang, H.-T. Carbon Nanotubes/Cobalt Sulfide Composites as Potential High-Rate and High-Efficiency Supercapacitors. *J. Power Sources* **2012**, *215*, 43–47.
11. Zhu, T.; Wu, H. B.; Wang, Y.; Xu, R.; Lou, X. W. Formation of 1D Hierarchical Structures Composed of Ni_3S_2 Nanosheets on CNTs Backbone for Supercapacitors and Photocatalytic H_2 Production. *Adv. Energy Mater.* **2012**, *2*, 1497–1502.
12. Zhang, G.; Lou, X. W. General Solution Growth of Mesoporous $NiCo_2O_4$ Nanosheets on Various Conductive Substrates as High-Performance Electrodes for Supercapacitors. *Adv. Mater.* **2013**, *25*, 976–979.
13. Yu, L.; Zhang, G.; Yuan, C.; Lou, X. W. Hierarchical Ni-Co_2O_4@MnO_2 Core−Shell Heterostructured Nanowire Arrays on Ni Foam as High-Performance Supercapacitor Electrodes. *Chem. Commun.* **2013**, *49*, 137–139.
14. Yuan, C.; Li, J.; Hou, L.; Zhang, X.; Shen, L.; Lou, X. W. Uitrathin Mesoporous $NiCo_2O_4$ Nanosheets Supported on Ni Foam as Advanced Electrodes for Supercapacitors. *Adv. Funct. Mater.* **2012**, *22*, 4592–4597.
15. Yan, J.; Fan, Z.; Sun, W.; Ning, G.; Wei, T.; Zhang, Q.; Zhang, R.; Zhi, L.; Wei, F. Advanced Asymmetric Supercapacitors Based on $Ni(OH)_2$/Graphene and Porous Graphene Electrodes with High Energy Density. *Adv. Funct. Mater.* **2012**, *22*, 2632–2641.
16. Lu, X.; Yu, M.; Wang, G.; Zhai, T.; Xie, S.; Ling, Y.; Tong, Y.; Li, Y. H-TiO_2@MnO_2//H-TiO_2@C Core−Shell Nanowires for High Performance and Flexible Asymmetric Supercapacitors. *Adv. Mater.* **2012**, *25*, 267–272.
17. Chen, P.-C.; Shen, G.; Shi, Y.; Chen, H.; Zhou, C. Preparation and Characterization of Flexible Asymmetric Supercapacitors Based on Transition-Metal-Oxide Nanowire/Single-Walled Carbon Nanotube Hybrid Thin-Film Electrodes. *ACS Nano* **2010**, *4*, 4403–4411.
18. Fan, Z.; Yan, J.; Wei, T.; Zhi, L.; Ning, G.; Li, T.; Wei, F. Asymmetric Supercapacitors Based on Graphene/MnO_2 and Activated Carbon Nanofiber Electrodes with High Power and Energy Density. *Adv. Funct. Mater.* **2011**, *21*, 2366–2375.
19. Jin, W.-H.; Cao, G.-T.; Sun, J.-Y. Hybrid Supercapacitor Based on MnO_2 and Columned FeOOH Using Li_2SO_4 Electrolyte Solution. *J. Power Sources* **2008**, *175*, 686–691.
20. Wang, Z.; Pan, L.; Hu, H.; Zhao, S. Co_9S_8 Nanotubes Synthesized on the Basis of Nanoscale Kirkendall Effect and Their Magnetic and Electrochemical Properties. *CrystEngComm* **2010**, *12*, 1899–1904.
21. Wang, L.; Liu, B.; Ran, S.; Huang, H.; Wang, X.; Liang, B.; Chen, D.; Shen, G. Nanorod-Assembled Co_3O_4 Hexapods with Enhanced Electrochemical Performance for Lithium-Ion Batteries. *J. Mater. Chem.* **2012**, *22*, 23541–23546.

22. Kung, C.-W.; Chen, H.-W.; Lin, C.-Y.; Huang, K.-C.; Vittal, R.; Ho, K.-C. CoS Acicular Nanorod Arrays for the Counter Electrode of an Efficient Dye-Sensitized Solar Cell. *ACS Nano* **2012**, *6*, 7016–7025.
23. El-Kady, M. F.; Strong, V.; Dubin, S.; Kaner, R. B. Laser Scribing of High-Performance and Flexible Graphene-Based Electrochemical Capacitors. *Science* **2012**, *335*, 1326–1330.
24. Yuan, L.; Lu, X.-H.; Xiao, X.; Zhai, T.; Dai, J.; Zhang, F.; Hu, B.; Wang, X.; Gong, L.; Chen, J.; *et al.* Flexible Solid-State Supercapacitors Based on Carbon Nanoparticles/MnO_2 Nanorods Hybrid Structure. *ACS Nano* **2011**, *6*, 656–661.
25. Kang, Y. J.; Chung, H.; Han, C. H.; Kim, W. All-Solid-State Flexible Supercapacitors Based on Papers Coated with Carbon Nanotubes and Ionic-Liquid-Based Gel Electrolytes. *Nanotechnology* **2012**, *23*, 065401.
26. Loussot, C.; Afanasiev, P.; Vrinat, M.; Jobic, H.; Leverd, P. C. Amorphous Cobalt Oxysulfide as a Hydrogen Trap. *Chem. Mater.* **2006**, *18*, 5659–5668.
27. Zhou, Y. X.; Yao, H. B.; Wang, Y.; Liu, H. L.; Gao, M. R.; Shen, P. K.; Yu, S. H. Hierarchical Hollow Co_9S_8 Microspheres: Solvothermal Synthesis, Magnetic, Electrochemical, and Electrocatalytic Properties. *Chem.—Eur. J.* **2010**, *16*, 12000–12007.
28. Tao, F.; Zhao, Y.-Q.; Zhang, G.-Q.; Li, H.-L. Electrochemical Characterization on Cobalt Sulfide for Electrochemical Supercapacitors. *Electrochem. Commun.* **2007**, *9*, 1282–1287.
29. Wang, B.; Park, J.; Su, D.; Wang, C.; Ahn, H.; Wang, G. Solvothermal Synthesis of CoS_2-Graphene Nanocomposite Material for High-Performance Supercapacitors. *J. Mater. Chem.* **2012**, *22*, 15750–15756.
30. Wang, Q.; Jiao, L.; Du, H.; Yang, J.; Huan, Q.; Peng, W.; Si, Y.; Wang, Y.; Yuan, H. Facile Synthesis and Superior Supercapacitor Performances of Three-Dimensional Cobalt Sulfide Hierarchitectures. *CrystEngComm* **2011**, *13*, 6960–6963.
31. Jiang, J.; Li, Y.; Liu, J.; Huang, X.; Yuan, C.; Lou, X. W. Recent Advances in Metal Oxide-Based Electrode Architecture Design for Electrochemical Energy Storage. *Adv. Mater.* **2012**, *24*, 5166–5180.
32. Xiao, X.; Ding, T.; Yuan, L.; Shen, Y.; Zhong, Q.; Zhang, X.; Cao, Y.; Hu, B.; Zhai, T.; Gong, L.; *et al.* WO_{3-x}/MoO_{3-x} Core/Shell Nanowires on Carbon Fabric as an Anode for All-Solid-State Asymmetric Supercapacitors. *Adv. Energy Mater.* **2012**, *2*, 1328–1332.
33. Tang, Z.; Tang, C.-h.; Gong, H. A High Energy Density Asymmetric Supercapacitor from Nano-architectured Ni$(OH)_2$/Carbon Nanotube Electrodes. *Adv. Funct. Mater.* **2012**, *22*, 1272–1278.
34. Chen, W.; Rakhi, R. B.; Hu, L.; Xie, X.; Cui, Y.; Alshareef, H. N. High-Performance Nanostructured Supercapacitors on a Sponge. *Nano Lett.* **2011**, *11*, 5165–5172.
35. Hu, L.; Chen, W.; Xie, X.; Liu, N.; Yang, Y.; Wu, H.; Yao, Y.; Pasta, M.; Alshareef, H. N.; Cui, Y. Symmetrical MnO_2—Carbon Nanotube—Textile Nanostructures for Wearable Pseudocapacitors with High Mass Loading. *ACS Nano* **2011**, *5*, 8904–8913.
36. Meng, F.; Ding, Y. Sub-Micrometer-Thick All-Solid-State Supercapacitors with High Power and Energy Densities. *Adv. Mater.* **2011**, *23*, 4098–4102.
37. Choi, B. G.; Chang, S.-J.; Kang, H.-W.; Park, C. P.; Kim, H. J.; Hong, W. H.; Lee, S.; Huh, Y. S. High Performance of a Solid-State Flexible Asymmetric Supercapacitor Based on Graphene Films. *Nanoscale* **2012**, *4*, 4983–4988.